Correlation Radiometry for Subcutaneous Temperature Measurements

Rob Streeter, *Graduate Student Member, IEEE*, Gabriel Santamaria Botello, Kaitlin Hall, *Graduate Student Member, IEEE*, and Zoya Popović, *Fellow, IEEE*

Abstract—This paper addresses microwave radiometry for passive noninvasive subcutaneous temperature measurements at a few centimeter depth. A correlation radiometer is designed from off-the-shelf parts to operate in the quiet 1.4-GHz band and tested on aqueous phantoms. The radiometer is first tested with a matched load, and then with a near-field planar probe antenna, both with two water phantoms of different volumes. The measurement resolution, sensitivity and long-term stability is quantified in terms of integration time for a simple three-point calibration. The lowest measured absolute error compared to a ground-truth thermocouple measurement is $\pm 0.25~\mathrm{K}$ over one hour of data collection with a single calibration. Measurements show that an integration time >1 s results in an absolute error limited by the radiometer gain fluctuations. A probe on a seven-layer tissue stack is designed for measuring brain temperature.

Index Terms—Correlation radiometer, thermometry, tissue temperature, patient monitoring.

I. INTRODUCTION

ETERMINATION and monitoring of internal body temperature is important for a number of medical diagnostic and treatment applications, including hyper-/hypo-thermia treatment [1], brain temperature monitoring [2]–[4], circadian cycle tracking [5], [6], heat-related injury mitigation [7], detection of arthritis/joint-inflammation [8], [9], and burn recovery monitoring [10], to name a few. Current technologies capable of detecting sub-cutaneous tissue temperature include invasive methods such as needles and catheters [11], [12] and radio pills [13]. Noninvasive methods such as zero heat flux [14], [15] and magnetic resonance imaging (MRI) [16] are bulky, expensive and power-hungry. A recent heat flux approach [17] appears to be wearable and is intended to measure skin temperature taking into account ambient temperature changes.

Often, particularly for estimating brain temperature, surrogate temperatures from more easily accessed locations on the body are measured [18]. To the best of the authors' knowledge, there are no currently available commercial devices capable

Manuscript received June 14, 2021; revised September 3, 2021; accepted October 7, 2021. This work was supported in part by the National Science Foundation (NSF) under Grant 2026523, and in part by the Lockheed Martin Endowed Chair and was submitted for review on June 14, 2021. (Corresponding author: Rob Streeter.)

The authors are with the University of Colorado at Boulder, Boulder, CO 80309 USA (e-mail: Robert.Streeter@colorado.edu; Gabriel.Santamaria Botello@colorado.edu; Kaitlin.Hall@colorado.edu; Zoya.Popovic@colorado.edu).

Digital Object Identifier 10.1109/JERM.2021.3120320

of directly measuring internal tissue temperature while also being mobile, low-power, easy to use, and with relatively low manufacturing costs. Microwave radiometry (MWR) offers a path to such a device. Non-wearable radiometers include those for breast cancer detection [19], astronaut monitoring [20], and brain temperature tracking [3]. Prototypes in [9], [21] describe wearable radiometers with calibration capability. The former is a clever compact design in the 3.5-4.1 GHz wide band where the sensing depth is relatively low due to tissue parameters in this frequency range.

A demonstration of microwave passive thermometry using tissue phantoms with sub-Kelvin relative temperature resolution is described in [22], where a Dicke radiometer is implemented with off-the-shelf components. Here, a correlation radiometer is introduced for sub-cutaneous thermometry, eliminating the need for a lossy switch and two calibration sources, along with associated control signals.

A block diagram of the setup used to characterize the microwave thermometer is shown in Fig. 1(b). The near-field probe antenna is mounted on the bottom of an EPS container filled with tap water. The correlation radiometer is designed to operate in the 27 MHz band beginning at 1.4 GHz, designated by the FCC as a "quiet band" for radio astronomy [23]. The dc output voltage of the detectors is digitized and used to estimate the temperature [22]. The temperature resolution of the radiometer is limited by the integration time and gain fluctuations of the low-noise amplifiers. Although the correlation radiometer architecture allows continuous calibration, here we investigate temperature estimation for the simplest case of a single calibration. By varying the integration time, the gain fluctuations, and therefore sensitivity, can be quantified.

The paper is organized as follows. A near-field probe designed for a specific water phantom is detailed in Section II, including simulations and measurements. The correlation radiometer implementation is described in Section III. Noise analysis, gain budget, and the calibration procedure are presented in Section IV. Experimental validation and temperature estimation is detailed in Section V, and Section VI shows a redesigned probe antenna on a seven-layer head tissue stack for brain temperature measurements.

II. NEAR-FIELD PROBE DESIGN

The near-field probe collects black-body thermal power from below the surface of a lossy dielectric (tissue) when it is

2469-7249 © 2021 IEEE. Personal use is permitted, but republication/redistribution requires IEEE permission. See https://www.ieee.org/publications/rights/index.html for more information.

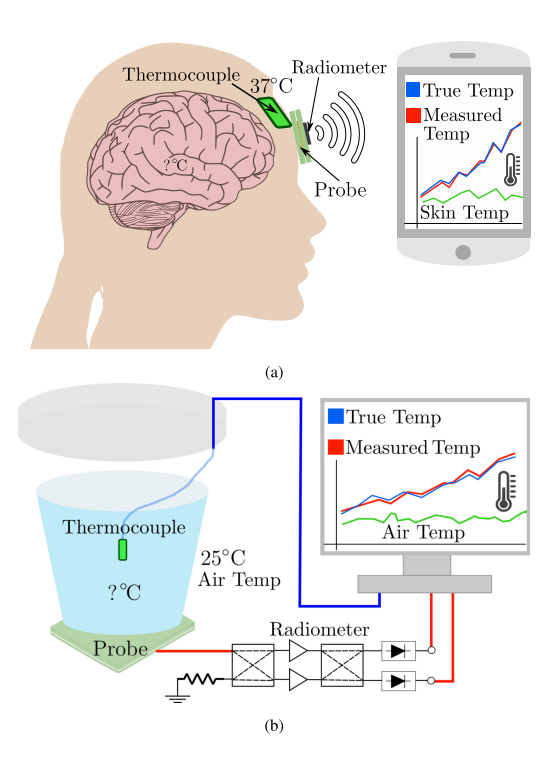


Fig. 1. (a) Illustration of one possible application of a wearable microwave radiometer: brain temperature measurements. (b) Aqueous phantom measurement setup with the correlation radiometer and near-field probe antenna. The radiometric temperature is compared with ground-truth thermocouple data.

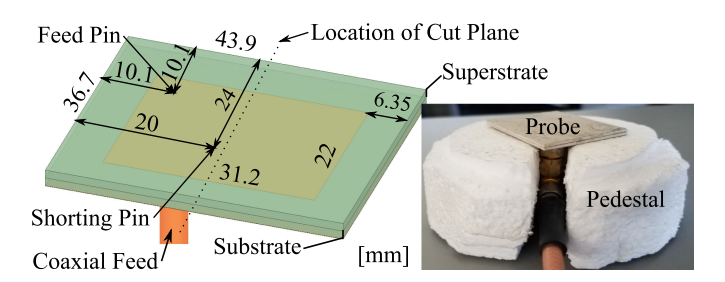


Fig. 2. The near-field probe is a corner-fed rectangular patch with a shorting pin. The patch is printed on 1.27 mm Rogers 6010.2LM ($\epsilon_r=10.2$). A superstrate of the same material is affixed using cyanoacrylate glue. Dimensions are in millimeters. The location of the cut plane for the overlays in Fig. 4 is shown. Inset: photo of the assembled probe and coaxial feed, along with the EPS pedestal used during measurements.

designed for a specific (possibly layered) material. Demonstrated printed probe topologies include taper-fed planar folded dipoles [24]–[27] which proved effective but had bulky feeds, as well as circular patches [27]–[29], coupled slots [30], and substrate-integrated waveguide slots [31]. Full waveguide topologies [32] are not feasible for wearable, long-term monitoring capable devices. The probe topology chosen for this work is a corner-fed rectangular patch, which maintains a high $\boldsymbol{E}_{\text{tan}}$ component, continuous across lossy dielectric boundaries. The probe is planar, thin and the ground plane helps mitigate RF interference. It is fabricated 1.27 mm thick Rogers 6010.2LM substrate and a includes superstrate of the same material and dimensions. An inductive shorting pin improves matching and further reduces the physical size of the probe [29], which is shown in Fig. 2.

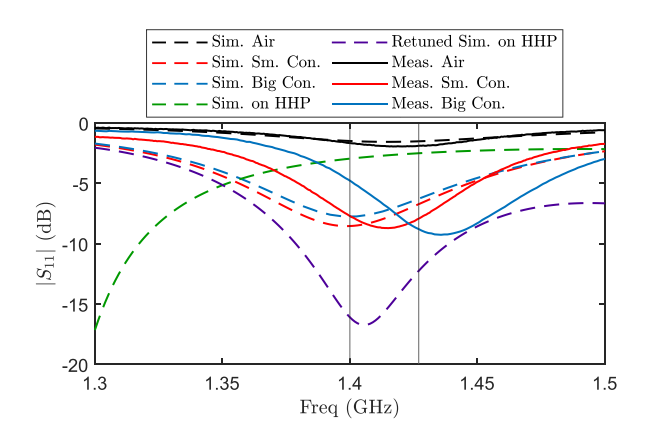


Fig. 3. Measured and simulated $|S_{11}|$ of the probe on water-filled EPS containers of different sizes. The simulated response of a redesigned probe for a head phantom (HHP) tissue stack [33], [34] is also shown. The return loss for a probe in air illustrates that a probe designed for a specific tissue stack does not function as a free-space antenna. The 27 MHz wide quiet band is indicated by the two vertical lines.

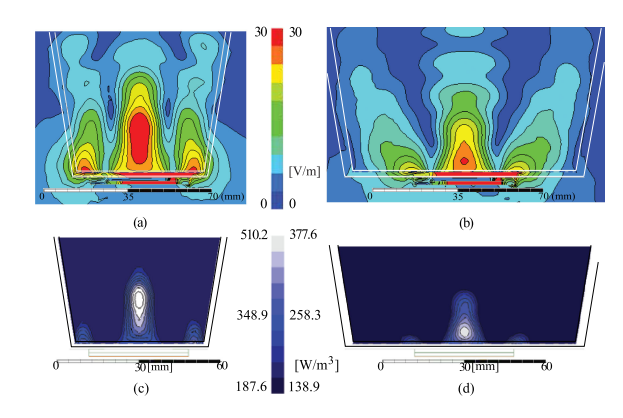


Fig. 4. Full-wave simulations at 1.412 GHz of (a,b) the **E**-field vector magnitude and (c,d) volume density of Joule losses for the rectangular probe placed on the bottom of the small (a,c) and large (b,d) EPS containers filled with cold tap water ($\epsilon_T = 86$, $\sigma = 1$ S/m).

We refer to the patch as a probe, since it is designed to perform with specific lossy dielectric layers in the near field, rather than in a free-space far field. For the measurements presented in this paper, the loading is tap water, with $\epsilon_r=86$ and $\sigma=1$ S/m, filling a 2-mm thick EPS ($\epsilon_r=1.03,\ \sigma=0$) container with base diameter, top diameter, and height of 50.8 mm, 90.5 mm, and 119 mm, respectively. We compare this initial setup with a larger EPS container with base and top diameters of 88.9 mm and 127 mm and 119 mm height. This corresponds to a 206% larger base surface area and a 130% larger volume for the larger container compared to the smaller one. Simulated and measured $|S_{11}|$ of the probe against a number of loadings is shown in Fig. 3. The mismatch presented by a probe at the input of the radiometer has to be corrected via calibration, and [21] includes a circulator to mitigate this issue.

Fig. 4 shows the results of full-wave electromagnetic simulations using Ansys HFSS of the largest cross-section of the two EPS containers. The E-field magnitudes (Fig. 4(a) and (b)) show some field outside of the water volume. The volume density of Joule losses, $p_{\rm J}=\sigma|E|^2$, is negligible in air outside the containers, and indicates that most of the thermal power

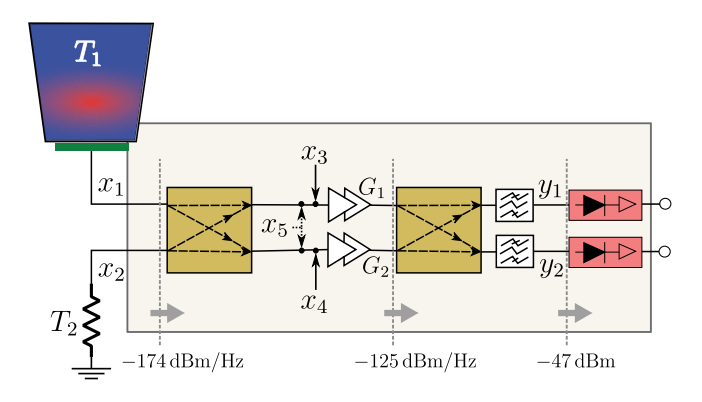


Fig. 5. Block diagram of the correlation radiometer. Physical temperatures $T_{1,2}$ produce time-varying noise signals $x_{1,2}$. The multi-stage LNAs $(G_{1,2})$, and the lossy input 90° coupler, add differential $(x_{3,4})$ and common-mode (x_5) noise into the signal path. After recombining and filtering, pre-detection signals $y_{1,2}$ are detected, amplified and digitized.

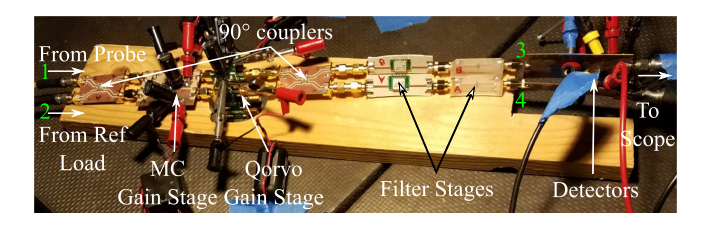


Fig. 6. The modular radiometer in an anechoic chamber. Thermal noise inputs from the probe and reference load arrive via coaxial cable at the first 90° coupler (ports 1 and 2; shown on the left) and move through the system from left to right. Ports 1–4 are labeled in green.

is received from a volume within the containers. The lines in Fig. 4(c) and Fig. 4(d) show this sensitive area, outside of which $p_{\rm J}$ drops below 1/e of the maximum. This volume is approximately 10.18 cm³ for the small container and 21.0 cm³ for the large container. The difference illustrates that a probe designed for a specific target performs differently on other materials.

 $p_{\rm J}$ is equivalent to the real part of the divergence of the Poynting vector. By reciprocity, the thermal noise power received by the probe is proportional to the power absorbed by the water if the probe were instead transmitting. Thus, the $p_{\rm J}$ plots (Fig. 4(c),(d)) represent a mapping of normalized received thermal power from the water phantom. It is worth noting that the "focusing" of $p_{\rm J}$ away from the bottom of the container is a consequence of reflections from the boundaries of the water. This effect is reduced with the larger container and is not present at all with sufficiently large water volumes. The probe in Fig. 2 is specifically designed for this test scenario and performance against other targets, including biological tissue stacks, will deviate from the results presented here (as shown by the "Head Phantom" trace in Fig. 3).

III. CORRELATION RADIOMETER DESIGN

A correlation radiometer shown in the block diagram of Fig. 5, and photo of Fig. 6, is implemented from off-the-shelf components, and the relevant power levels are given in Fig. 5, assuming room temperature ($T=300\,\mathrm{K}$) inputs. A correlation topology is selected over the Dicke [24], [35] for the following reasons:

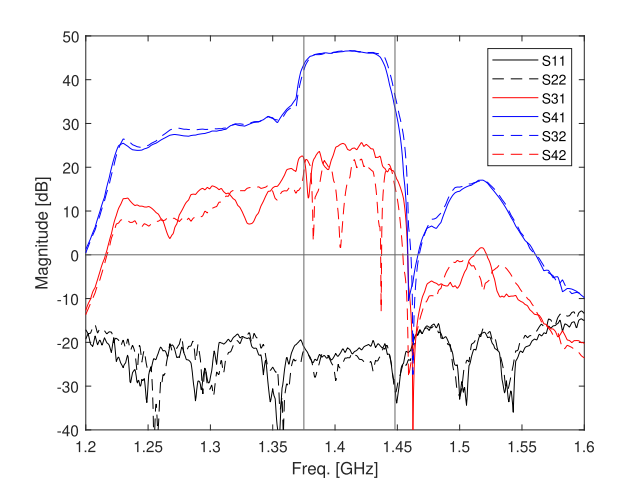


Fig. 7. Circuit simulation in Cadence's AWR of the RF chain S-parameter magnitudes using measured values. The vertical lines indicate the 72.2 MHz power-equivalent bandwidth. Fig. 6 provides references for port designations.

- The correlation topology eliminates the RF switch, which is a source of loss and therefore noise, and requires continuous additional control signals;
- The duty cycle on-target is 100% compared to 50% (or less), simplifying the post-processing and expediting the observation time needed for a calibrated measurement;
- The output signal is differential, improving robustness to EMI through common-mode rejection.

Referring to Figs. 5 and 6, one of the input coupler ports (x_1) is connected to the probe and target, while the other port (x_2) is connected to a calibration reference at known temperature T_2 . Time-varying thermal noise signals from the two input ports of the 90°-hybrid are combined linearly, amplified with multi-stage low-noise amplifiers (LNAs) and recombined with commonmode rejection of RFI and LNA noise temperature drift. The current experiments use Anaren XC1400P-03S couplers. While 180°-hybrids are common in the literature, 90°-hybrids are selected for this design based on their smaller size and the analysis in [36]. The difference between the RF power of the output signals is proportional to the difference between the input noise temperatures of the probe and known calibration reference. Before detection, the signals are filtered using Mini-Circuits' CBP-1400E+ ceramic coaxial filters followed by Tai-Saw Tech TA2313 A surface acoustic wave (SAW) filters with a total insertion loss of $\sim 2.6 \, \mathrm{dB}$ and central frequency $f_0 = 1.412 \, \mathrm{GHz}$. From the measured normalized power transfer function H(f)we determine a FWHM bandwidth of 63.43 MHz, which corresponds to a power-equivalent bandwidth $\Delta f = \int_0^\infty H(f) df =$ 72.2 MHz. Note that the couplers are well-balanced in both magnitude and phase within the 72.2 MHz observation bandwidth. Fig. 7 shows the simulated 4-port RF chain with measured values. The observation bandwidth is determined by the narrowband SAW filters. Out-of-band gain is reduced by up to 8 dB by the resonant detector matching circuit.

The received thermal noise power from room-temperature ($T \approx 300\,\mathrm{K}$) input sources is on the order of $kT\Delta f \approx -95\,\mathrm{dBm}$, where k is Boltzmann constant, and Δf the reception

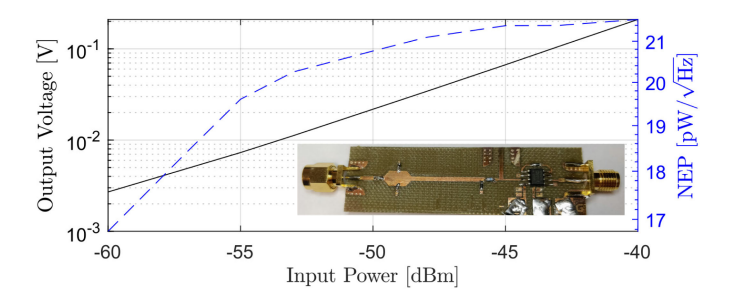


Fig. 8. Measured voltage reponsivity and noise-equivalent power (NEP) of the detector at 1.412 GHz. Inset: photograph of the detector with high-Q resonator and post-detection amplification of ~ 100 .

bandwidth. Thus, taking into account losses in the system, approximately 50 dB of gain is needed to amplify the signals sufficiently above the minimum detectable range of the square-law detectors. We use a Mini-Circuits TAMP1521GLN+ cascaded with a Qorvo TQP3M9036 amplifier. The noise figure of the first stage is 0.58 dB with 35 dB of gain, making the impact of the second-stage noise figure negligible. The stability of the LNA chain is influenced by all stages, as well as coupler isolation, chosen to be >20 dB. Bias circuit design is critical for stability; 200 nH series inductors with 2.2 mF decoupling capacitors near the LNAs are included in both stages.

The detectors are designed with Skyworks SMS7630-079 diodes, with a matching circuit consisting of a $\lambda/4$ resonator coupled through shunt capacitors. This matches the impedance of the diode within $\sim\!60\,\mathrm{MHz}$ around $1.412\,\mathrm{GHz}$. The rectified voltage is amplified by a post-detection gain stage with G $\sim\!100$. The detectors exhibit a post-amplification responsivity better than $2.8\,\mathrm{MV/W}$ and a NEP $<22\,\mathrm{pW/\sqrt{Hz}}$ at $1.412\,\mathrm{GHz}$ over the input power range -60 to -40 dBm. V_rms and half-power bandwidth (HPBW; $20\,\mathrm{kHz}$) is measured post-amplification for this input power range. The instrument (a two-channel Agilent InfiniiVision DSO-X 2022 A oscilloscope) noise floor voltage is $V_\mathrm{flr} = 6.4\,\mathrm{mV}$. The normalized NEP can then be computed as:

$$NEP = \frac{V_{flr}}{V_{rms}} \frac{P_{in}}{\sqrt{HPBW}}$$
 (1)

where $P_{\rm in}$ is in watts and HPBW in Hz, as shown in Fig. 8.

IV. CALIBRATION ANALYSIS

Ideally, the dual coupler configuration in Fig. 5 combines the two inputs with appropriate phases such that each one exits through a single output of the radiometer, along with equal-power noise introduced by the LNAs. Since all noise sources are uncorrelated, the difference of mean power measured at the radiometer outputs is proportional to the difference in input temperatures $T_2 - T_1$, and the proportionality constant can be measured by calibrating the radiometer with two known input temperatures. However, slight imbalances in the system break this proportionality, requiring a more complete calibration.

A. Mean Output Power

To find the power at the output of a realistic correlation radiometer, referring to Fig. 5, we assume that the input bandlimited noise signals are complex Gaussian processes $x_{1,2}(t)$ that represent slow-varying amplitudes of the electromagnetic fields (or voltages/currents) at 1.412 GHz. The noise temperature of each LNA is accounted for by introducing noise sources $x_{3,4}(t)$ at their inputs. Input coupler loss also introduces thermal noise, while post-amplification output coupler noise is negligible. This added noise is split into two uncorrelated components at the coupler outputs, added to $x_{3,4}(t)$, and a component $x_5(t)$ common to both branches. Amplitudes $x_k(t)$, k = 1...5 are statistically independent and normalized such that $|x_k(t)|^2$ gives the corresponding cycle-averaged power. Since the spectral characteristics of the radiometer outputs are mostly determined by the narrowband SAW filters, all noise sources $x_k(t)$ are defined such that their power spectral densities follow H(f).

Assuming all devices are well matched and the spectral response of the couplers and LNAs is approximately flat over Δf , we can write the radiometer outputs $y_{1,2}(t)$ as linear combinations of all noise sources:

$$y_j(t) = \sum_{k=1}^{5} a_{jk} x_k(t) \quad j = 1, 2.$$
 (2)

The coefficients $a_{jk}(t)$ are in general functions of time because the gain of the amplifiers $g_{1,2}(t)$ fluctuates. Since all noise sources $x_k(t)$ and gain fluctuations $g_{1,2}(t)$ are uncorrelated processes, the mean power at the radiometer outputs is:

$$\overline{P_j} = \left\langle |y_j(t)|^2 \right\rangle = \sum_{k=1}^5 \left\langle |a_{jk}(t)|^2 \right\rangle \left\langle |x_k(t)|^2 \right\rangle, \tag{3}$$

where the $\langle \cdot \rangle$ operator indicates expected value. It can be shown that when the couplers are ideal, and LNA gains equal $(|g_1|^2 = |g_2|^2 = G)$, Eqn. (3) reduces to

$$\overline{P_j} = k\Delta fG\left(T_{3-j} + \frac{1}{2}T_3 + \frac{1}{2}T_4\right), \quad j = 1, 2$$
 (4)

where a temperature T_k is defined for all noise powers as $\left\langle |x_k(t)|^2 \right\rangle = kT_k\Delta f$, and $x_5=0$ because ideal couplers are lossless. Eqn. (4) shows that in an ideal correlation radiometer, the difference in the input temperatures can be retrieved by taking the difference of the average output powers, provided that $G\Delta f$ is known. This provides immunity against common noise sources such as RFI and LNA noise. The bandwidth-gain product can be obtained experimentally by characterizing the radiometer with two known temperatures T_1 and T_2 , and solving for $G\Delta f$ in Eqn. (4), known as the Y-factor technique. To find unknown coefficients that result from radiometer imperfections, a characterization with three known temperatures is performed, discussed next.

B. Three-Point Calibration

Temperature retrieval from (4) is not accurate for a non-ideal radiometer. Instead, we rely on Eqn. (3) and recognize that in the absence of RFI, the mean power measured at each output of the

radiometer is a linear combination of the two inputs and an offset term dependent on the LNA cascade noise figure and non-ideal coupler characteristics, i.e., $\overline{P_j} = \alpha_{j1}T_1 + \alpha_{j2}T_2 + \alpha_{j3}, \ j = 1,2.$ The mean voltages $\overline{V_j}$ at the outputs of the square-law detectors are proportional to $\overline{P_j}$, and the proportionality constant is absorbed in α_{jk} . Zero-mean white noise from the detectors does not contribute to $\overline{V_j}$ (although it increases the fluctuations of V_j), and any offset voltage can be included into α_{j3} .

In order to mitigate RFI and LNA noise temperature drifts encoded into α_{j3} , the system of equations is rewritten in terms of the difference in the outputs: $\overline{V_2} - \overline{V_1} = \Delta_1 T_1 + \Delta_2 T_2 + \Delta_3$, where $\Delta_1 = \alpha_{21} - \alpha_{11}$, $\Delta_2 = \alpha_{22} - \alpha_{12}$, and $\Delta_3 = \alpha_{23} - \alpha_{23}$ α_{13} . Thus, there are three unknowns $\Delta_{1,2,3}$ that are constant for a given prototype. However, a measurement is carried out during a finite time τ , and estimations of V_j are only as accurate as determined by τ . For this reason, gain fluctuations that are slow compared to τ produce changes in the coefficients, potentially making periodic calibrations necessary. The impact of the sample integration time, τ , is discussed in greater detail in Section V. Three pairs of known input temperatures $(T_1^{(i)}, T_2^{(i)}), i = 1, 2, 3$, chosen over a wide range, are used to solve for the calibration coefficients $\Delta_{1,2,3}$ that characterize the radiometer. With a reference load at a known temperature T_2 , the radiometer can be used to estimate an unknown temperature

$$T_1^{\text{estim}} = \frac{\overline{V_2} - \overline{V_1} - \Delta_2 T_2 - \Delta_3}{\Delta_1}.$$
 (5)

V. CHARACTERIZATION AND MEASUREMENTS

To evaluate the behavior and accuracy of the radiometer only, we first characterize it without the probe. The radiometer is calibrated in an anechoic chamber by connecting to the inputs two matched loads immersed in two water baths with different physical temperatures. The temperatures are tracked with thermocouples co-located with the immersed loads. At the same time, both outputs of the radiometer are digitized with the same Agilent oscilloscope listed previously, at a sampling rate of $1\,\mathrm{GHz}$, fast enough to track the signal coming out of the detectors, whose instantaneous bandwidth is about $20\,\mathrm{kHz}$. However, the samples are internally averaged by the oscilloscope with an integration time $\tau=2\,\mathrm{ms}$ and are then read and stored by a MATLAB script controlling the scope.

Three tests were performed with different initial water temperatures, $(T_1, T_2) = (81.39, 74.44)$ °C; (48.72, 25.55) °C; (24.73, 3.32) °C. The water was left to cool down or warm up to ambient temperature (about 16 °C). Temperature gradients inside the water are expected, which presents a source of estimation error when the localized temperature of a thermocouple is compared to the weighted volumetric average received by the near-field probe.

The raw time series of the oscilloscope voltages and thermocouple temperatures are time-aligned, and are shown in Fig. 9 for all three tests. The output voltage difference V_1-V_2 , proportional to P_1-P_2 averaged during τ , in the ideal case tracks the difference in physical temperature. For a realistic radiometer, Fig. 9 shows that the two data sets are not exactly proportional.

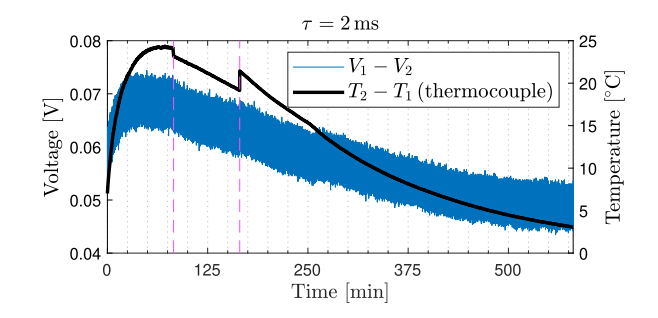


Fig. 9. Difference in raw temperatures and voltages acquired for three different experiments, each separated by dashed, vertical lines. It is evident how V_1-V_2 and T_2-T_1 are not exactly proportional, since the radiometer and experimental setup are not perfect. The integration time is $\tau=2\,\mathrm{ms}$.

Therefore, a three-point calibration is done by choosing three samples of voltages $V_{1,2}$, and thermocouple temperatures $T_{1,2}$ at instants $t_1=2\min$, $t_2=180\min$ and $t_3=370\min$ and calculating the coefficients $\Delta_{1,2,3}$. Times $t_{1,2,3}$ are chosen to cover a wide range of temperatures, in which case their choice does not impact the results significantly.

Using the calibration coefficients and the thermocouple temperature T_2 , the unknown temperature T_1 is estimated via Eqn. (5) and compared to the value of T_1 measured with the thermocouple. This is shown in Fig. 10 for different integration times τ , ranging from the internal averaging of the oscilloscope ($\tau = 2 \,\mathrm{ms}$) up to $\tau = 5 \,\mathrm{s}$. For $\tau > 2 \,\mathrm{ms}$, the raw data is averaged further in post-processing. Increasing the integration time τ significantly improves the accuracy, as expected since the radiometric uncertainty scales $\propto (B\tau)^{-1/2}$, where $B \approx \Delta f$ is the noise equivalent bandwidth [37]. However, increasing τ above about 1 s, although smoothing the results, does not reduce the absolute error in the temperature estimation. This is illustrated in Fig. 11, which shows the spectral noise content of $V_2 - V_1$, and indicates a knee frequency between 1/f noise and thermal noise at about 0.4 Hz, or $\tau \sim 1.25\,\mathrm{s}$. In the measurements in Fig. 10, the accuracy saturates at about $\Delta T = \pm 2$ °C. This implies that gain fluctuations (with a 1/f-like spectrum) dominate the radiometric fluctuations and the overall system uncertainty. For $\tau = 5 \,\mathrm{s}$, $\Delta T = 2 \,^{\circ}\mathrm{C}$ is the absolute temperature resolution achieved with a single calibration over ~ 10 hours of measurements. Note that the observed gain fluctuations are slow and can be mitigated by periodic calibration. The data suggests that performing periodic calibrations every minute would reduce the absolute temperature uncertainty to about $\Delta T \approx 0.2$ °C.

The procedure described above is followed to calibrate the radiometer with the probe connected to one input (T_1) while the other input is connected to a matched-load temperature reference immersed in a water bath (T_2) . For these measurements, the probe is attached to the outside base of the smaller water-filled EPS container. Two thermocouples measure physical temperatures of the reference load and the unknown water phantom sensed by the probe.

The thermocouple measured initial aqueous phantom temperature is $T_1=47.88\,^{\circ}\mathrm{C}$, and the reference load water temperature is $T_2=28.30\,^{\circ}\mathrm{C}$. The water is allowed to cool down to ambient of $\sim\!16\,^{\circ}\mathrm{C}$ while data is acquired. A single calibration is performed by choosing three samples at points $t_1=10\,\mathrm{min}$,

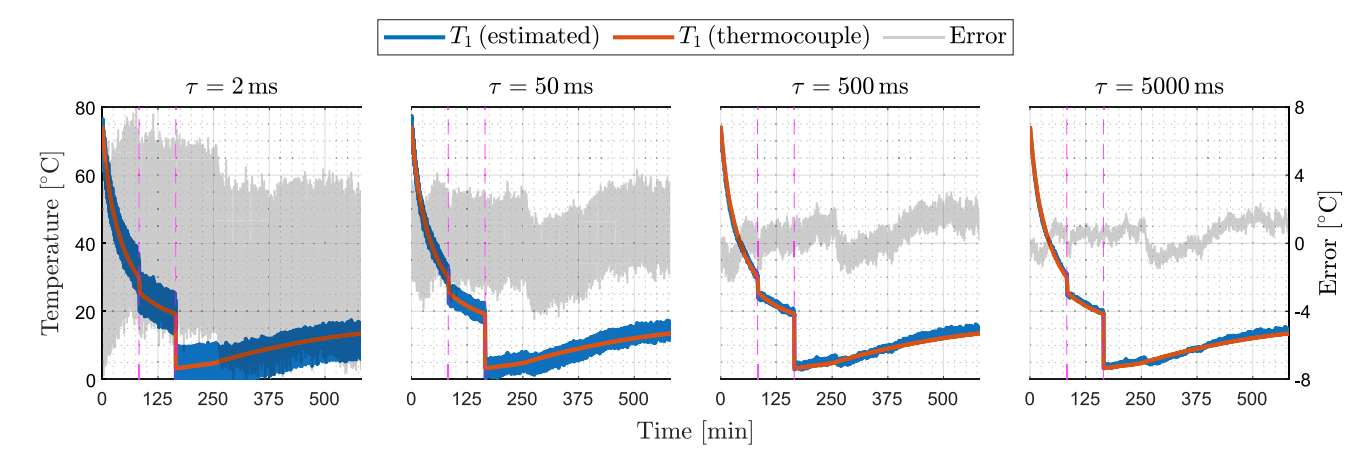


Fig. 10. Estimated T_1 vs ground-truth measured by thermocouple for different integration times τ and the three experiments shown in Fig. 9 (separated by the dashed, vertical lines). A single calibration is performed with three data samples, and the same resulting coefficients $\Delta_{1,2,3}$ are used to estimate the temperature over the \sim 10 hour long dataset.

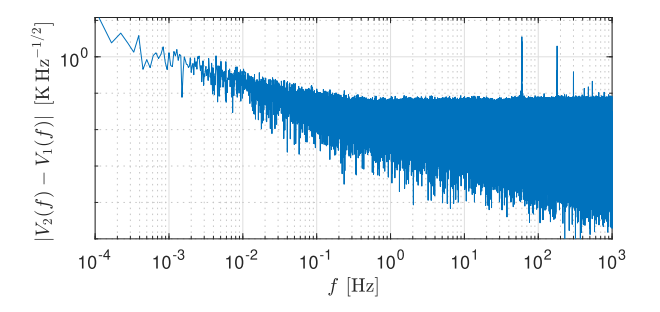


Fig. 11. Noise spectral content of V_2-V_1 , sampled over five hours with $\tau=0.4\,\mathrm{ms}$. A knee at 0.4 Hz shows the transition between 1/f and thermal noise and aligns with our empirical results: an integration time, $\tau\gtrsim1.25\,\mathrm{s}$, smooths the result but does not improve radiometer performance. The spikes at higher frequencies are supply-line noise.

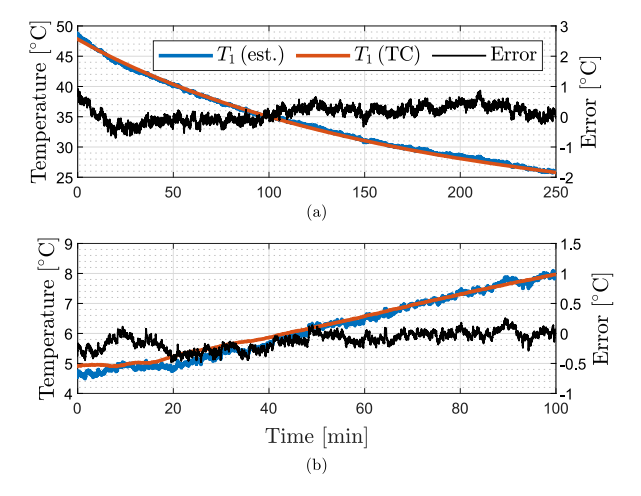


Fig. 12. Estimated water temperature vs ground-truth thermocouple measurement. The water temperature is sensed by attaching the probe at the base of water-filled small (a) and large (b) containers. Note the different scales. In each case, a single three-point calibration is used for the complete dataset.

 $t_2=80\,\mathrm{min}$ and $t_3=250\,\mathrm{min}$, and the resulting coefficients $\Delta_{1,2,3}$ are used to estimate the probe-sensed water temperature. The results are plotted in Fig. 12(a), showing a maximal absolute error within $\Delta T<0.87\,^{\circ}\mathrm{C}$.

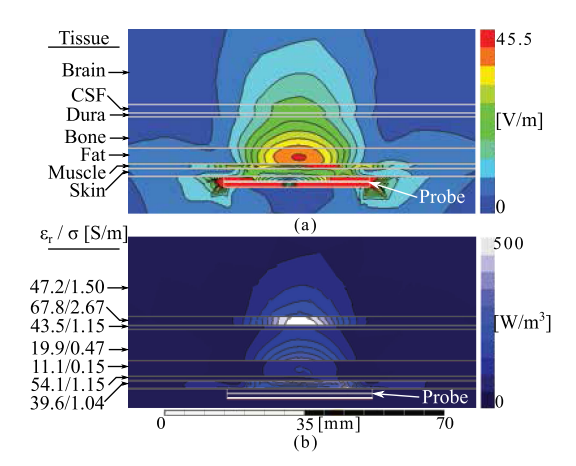


Fig. 13. Full-wave simulations of (a) **E**-field magnitude and (b) volume density of Joule losses (with high values in the cerebrospinal fluid - CSF - layer) of a probe designed for the 7-layer "forehead" tissue stack of [33], [34]. This probe is redesigned from that of Fig. 2: the shorting pin is removed and the dimensions adjusted. The 1/e threshold volume is about 14.71 cm³. Tissue properties at 1.412 GHz are provided for reference.

Another probe characterization is performed, this time with a large EPS container. The initial temperatures of water in the probe cup and reference load are $T_1=4.92\,^{\circ}\mathrm{C}$, and $T_2=56.06\,^{\circ}\mathrm{C}$, respectively. Calibration is carried out with samples at times $t_1=10\,\mathrm{min}$, $t_2=50\,\mathrm{min}$ and $t_3=100\,\mathrm{min}$, and the estimation of the probe temperature is shown in Fig. 12(b). The resulting absolute error is within $\Delta T<0.48\,^{\circ}\mathrm{C}$, and an error of $\Delta T<0.25\,^{\circ}\mathrm{C}$ over the last hour of data collection.

VI. CONCLUSION

This paper demonstrates microwave radiometry for passive, noninvasive subsurface temperature measurements with a correlation radiometer in the quiet 1.4 GHz band. The radiometer is tested with a matched load at different temperatures to evaluate calibration. A planar near-field probe is designed and analyzed against aqueous phantoms. For a wearable application, a specific probe is designed on a 7-layer tissue stack of a typical forehead, described in [33], [34]. The probe has a similar geometry as

the one in Fig. 2, with modified dimensions. The resulting E-field and $p_{\rm J}$ are shown in Fig. 13. Peak thermal power is received from the brain and cerebrospinal fluid (CSF), as well as from the skin. The CSF is expected to be at nearly the same temperature as the brain. Either probe can be connected to the radiometer, which is experimentally characterized in terms of accuracy. The lowest measured absolute error compared to a ground-truth thermocouple measurement is $\pm 0.25\,\rm K$ over one hour of data collection with a single three-point calibration. Noise analysis shows that an integration time of $>1~\rm s$ results in an absolute error limited by the radiometer flicker noise. The correlation topology enables extensions to a pseudo-correlation radiometer [38], which would allow periodic calibration for increased accuracy. Both topologies can be integrated on-chip for further miniaturization and RFI mitigation.

REFERENCES

- [1] M. Bommadevara, "Temperature difference between the body core and arterial blood supplied to the brain during hyperthermia or hypothermia in humans," *Biomech. Model. Mechanobiol.*, vol. 1, no. 2, pp. 137–149, 2002.
- [2] S. Rossi, E. R. Zanier, I. Mauri, A. Columbo, and N. Stocchetti, "Brain temperature, body core temperature, and intracranial pressure in acute cerebral damage," *J. Neurol., Neurosurgery Psychiatry*, vol. 71, no. 4, pp. 448–454, 2001.
- [3] P. R. Stauffer et al., "Non-invasive measurement of brain temperature with microwave radiometry: Demonstration in a head phantom and clinical case," *Neuroradiol. J.*, vol. 27, no. 1, pp. 3–12, Feb. 2014.
- [4] T. Sugiura et al., "Five-band microwave radiometer system for non-invasive measurement of brain temperature in new-born infants: System calibration and its feasibility," in Proc. 26th Annu. Int. Conf. IEEE Eng. Med. Biol. Soc., 2004, vol. 1, pp. 2292–2295.
- [5] J. Waterhouse *et al.*, "The circadian rhythm of core temperature: Origin and some implications for exercise performance," *Chronobiol. Int.*, vol. 22, no. 2, pp. 207–225, 2005.
- [6] S. Mendt et al., "Circadian rhythms in bed rest: Monitoring core body temperature via heat-flux approach is superior to skin surface temperature," *Chronobiol. Int.*, vol. 34, no. 5, pp. 666–676, 2017. [Online]. Available: https://doi.org/10.1080/07420528.2016.1224241
- [7] A. S. Howe and B. P. Boden, "Heat-related illness in athletes," Amer. J. Sports Med., vol. 35, no. 8, pp. 1384–1395, 2007.
- [8] K. Laskari et al., "Joint microwave radiometry for inflammatory arthritis assessment," Rheumatology, vol. 59, no. 4, pp. 839–844, 09 2019. [Online]. Available: https://doi.org/10.1093/rheumatology/kez373
- [9] V. M. Ravi, A. K. Sharma, and K. Arunachalam, "Pre-clinical testing of microwave radiometer and a pilot study on the screening inflammation of knee joints," *Bioelectromagnetics*, vol. 40, no. 6, pp. 402–411, Sep. 2019.
- [10] A. Owda, N. Salmon, S. Shylo, and M. Owda, "Assessment of bandaged burn wounds using porcine skin and millimetric radiometry," *Sensors*, vol. 19, no. 13, p. 2950, 2019.
- [11] D. Camboni, A. Philipp, K.-M. Schebesch, and C. Schmid, "Accuracy of core temperature measurement in deep hypothermic circulatory arrest," *Interactive CardioVasc. Thoracic Surgery*, vol. 7, no. 5, pp. 922–924, Oct. 2008.
- [12] E. Schena et al., "Solutions to improve the outcomes of thermal treatments in oncology: Multipoint temperature monitoring," *IEEE J. Electromagn.*, *RF, Microw. Med. Biol.*, vol. 2, no. 3, pp. 172–178, Sep. 2018.
- [13] C. C. Bongers, M. T. Hopman, and T. M. Eijsvogels, "Using an ingestible telemetric temperature pill to assess gastrointestinal temperature during exercise," *J. Visualized Exp.*, Oct. 2015, Art. no. 53258. [Online]. Available: https://www.ncbi.nlm.nih.gov/pmc/articles/PMC4692644/pdf/jove-104-53258.pdf
- [14] Y. Eshraghi et al., "An evaluation of a zero-heat-flux cutaneous thermometer in cardiac surgical patients," *Anesthesia Analgesia*, vol. 119, no. 3, pp. 543–549, 2014.
- [15] S. Mazgaokera, I. Ketkoa, R. Yanovicha, Y. Heled, and Y. Epstein, "Measuring core body temperature with a non-invasive sensor," *J. Thermal Biol.*, vol. 66, pp. 17–20, 2017.

- [16] S. Sheehan, "Accurate temperature imaging based on intermolecular coherence in magnetic resonance," *Science*, vol. 322, no. 5900, pp. 421–424, Oct. 2008.
- [17] CORE venture, "Continuous core body temperature monitoring," Oct. 2021. Accessed: Oct. 25, 2021. [Online]. Available: https://www.greenteg. com/template/userfiles/files/CORE-SpecSheet-V1.9.8.pdf
- [18] J. L. Robinson, R. F. Seal, D. W. Spady, and M. R. Joffres, "Comparison of esophageal, rectal, axillary, bladder, tympanic, and pulmonary artery temperatures in children," *J. Pediatrics*, vol. 133, no. 4, pp. 553–556, 1998. [Online]. Available: https://www.sciencedirect.com/science/article/ pii/S0022347698700678
- [19] REDLtd, "RTM-01-RES," 2001. Accessed: Oct. 25, 2021. [Online]. Available: http://www.resltd.ru/eng/rtm/
- [20] A. C. Stahn et al., "Increased core body temperature in astronauts during long-duration space missions," *Nature*, vol. 7, pp. 1–8, Nov. 2017.
- [21] S. G. Vesnin et al., "Portable microwave radiometer for wearable devices," Sensors Actuators A: Phys., vol. 318, 2021, Art. no. 112506. [Online]. Available: https://www.sciencedirect.com/science/article/pii/S0924424720318215
- [22] P. Momenroodaki, W. Haines, M. Fromandi, and Z. Popovic, "Noninvasive internal body temperature tracking with near-field microwave radiometry," *IEEE Trans. Microw. Theory Techn.*, vol. 66, no. 5, pp. 2535–2545, May 2018.
- [23] Federal Communications Commission, 47 C.F.R. § 2.106, FCC Online Table of Frequency Allocations, Feb. 2021. Accessed: Oct. 25, 2021. [Online]. Available: https://transition.fcc.gov/oet/spectrum/table/fcctable.pdf
- [24] R. P. Scheeler, "A microwave radiometer for internal body temperature measurement," Ph.D. dissertation, Univ. Colorado Boulder, Boulder, CO, USA, 2013.
- [25] Z. Popovic, P. Momenroodaki, and R. Scheeler, "Toward wearable wireless thermometers for internal body temperature measurements," *IEEE Commun. Mag.*, vol. 52, no. 10, pp. 118–125, Oct. 2014.
- [26] R. Scheeler, E. F. Kuester, and Z. Popović, "Sensing depth of microwave radiation for internal body temperature measurement," *IEEE Trans. Antennas Propag.*, vol. 62, no. 3, pp. 1293–1303, Mar. 2014.
- [27] P. Momenroodaki, Z. Popovic, and R. Scheeler, "A 1.4-GHz radiometer for internal body temperature measurements," in *Proc. Eur. Microw. Conf.*, 2015, pp. 694–697.
- [28] P. Momenroodaki and Z. Popović, "Antenna probes for power reception from deep tissues for wearable microwave thermometry," in *Proc. IEEE Int. Symp. Antennas Propag. USNC/URSI Nat. Radio Sci. Meeting*, San Diego, CA, 2017, pp. 573–574.
 [29] P. Momenroodaki, "Radiometric thermometry for wearable deep tissue
- [29] P. Momenroodaki, "Radiometric thermometry for wearable deep tissue monitoring," Ph.D. dissertation, Univ. Colorado Boulder, Boulder, CO, USA, 2017.
- [30] Y. S. Koo, "Wide band embedded slot antennas for biomedical, harsh environment, and rescue applications," Ph.D. dissertation, Univ. Tennessee-Knoxville, Knoxville, TN, USA, 2015.
- [31] V. M. Ravi and K. Arunachalam, "SIW slot antenna for passive measurement of thermal anomalies in biological tissues," *IET Microw., Antennas Propag.*, vol. 12, no. 7, pp. 1048–1053, 2018. [Online]. Available: https://ietresearch.onlinelibrary.wiley.com/doi/abs/10.1049/iet-map.2017.0340
- [32] M. K. Sedankin, I. V. Nelin, V. Y. Leushin, V. A. Skuratov, L. Y. Mershin, and S. G. Vesnin, "System of rational parameters of antennas for designing a multi-channel multi-frequency medical radiometer," in *Proc. Int. Conf. Actual Problems Electron Devices Eng.*, 2020, pp. 154–159.
- [33] A. Drossos, V. Santomaa, and N. Kuster, "The dependence of electromagnetic energy absorption upon human head tissue composition in the frequency range of 300–3000 MHz," *IEEE Trans. Microw. Theory Techn.*, vol. 48, no. 11, pp. 1988–1995, Nov. 2000.
- [34] B. A. Lloyd, "Virtual population: Tissue properties: Dielectric properties. IT'IS Foundation," 2021. Accessed: Oct. 25, 2021. [Online]. Available: https://itis.swiss/virtual-population/tissue-properties/database/dielectric-properties/
- [35] D. F. Wait, "The sensitivity of the Dicke radiometer," *J. Res. Nat. Bur. Standards*, vol. 71, no. 2, pp. 127–152, Jan. 1967.
- [36] A. I. Harris, "Spectroscopy with multichannel correlation radiometers," *Rev. Sci. Instrum.*, vol. 76, no. 5, 2005, Art. no. 054503. [Online]. Available: https://doi.org/10.1063/1.1898643
- [37] M. Tiuri, "Radio astronomy receivers," *IEEE Trans. Antennas Propag.*, vol. 12, no. 7, pp. 930–938, Dec. 1964.
- [38] A. Mennella et al., "Offset balancing in pseudo-correlation radiometers for CMB measurements," Astron. Astrophys., vol. 410, pp. 1089–1100, 2003.



Rob Streeter (Graduate Student Member, IEEE) received the B.S. degree in electrical and computer engineering from the University of Wyoming, United States, in 2011, and the M.S. degree in electrical engineering from the University of Wyoming, United States, in 2013. He has worked on UAS decision-making algorithms and test protocols for the U.S. Air Force Academy as a Research Engineer, LMR and IP system design, deployment, and maintenance for public and private entities with Ryan Electronics, Inc., and in 2017/18 was a winter-over Research Associate

with the Amundsen-Scott South Pole Station (under employment by Leidos for the Antarctic Support Contract, which is operated by the NSF). His research interests include engineering education and interdisciplinary, including medical, applications of electrical engineering principles.



Kaitlin L. Hall (Graduate Student Member, IEEE) received the B.S. degree in electrical engineering from the University of Utah, Salt Lake City, UT, USA, in 2020. She is currently working toward the Ph.D. degree in electrical engineering from the University of Colorado at Boulder, Boulder, CO, USA in the area of microwave radiometry for medical applications. She previously conducted research on implantable antennas, RFID antennas, and material properties of the human body at the University of Utah. Her research interests include bioelectromagnetics, microwave ra-

diometry, noninvasive brain stimulation, and engineering education for students with disabilities. She is a 2021 NSF GRFP fellow and was the recipient of the IEEE APS Pre-Doctoral Research Award in 2019.



Gabriel Santamaria Botello received the Electrical Engineering degree from the University of Carabobo, Venezuela in 2014 after completing his final project on the development of a full-wave electromagnetic solver based on the multi-level fast multipole method (MLFMM). In 2015, he joined the Group of Radiofrequency, Electromagnetism, Microwaves, and Antenas at Charles III University of Madrid (UC3M) and received the Ph.D. degree in January 2021. His Ph.D. thesis mainly focused on the theoretical analysis of THz-to-optical upconversion via resonant electro-

optics techniques for high sensitivity THz radiometry. He is currently working on RF field sensing techniques using Rydberg atoms and the development of non-invasive radiometers for internal body temperature measurements.



Zoya Popović (Fellow, IEEE) received the Dipl.Ing. degree from the University of Belgrade, Serbia, and the Ph.D. degree from Caltech, United States. She is a Distinguished Professor and the Lockheed Martin Endowed Chair in Electrical Engineering with the University of Colorado, Boulder. She was a Visiting Professor with the Technical University of Munich in 2001/03, ISAE in Toulouse, France in 2014, and was the Chair of Excellence at Carlos III University in Madrid in 2018/19. She has graduated more than 65 Ph.D.s and currently advises 17 doctoral students.

Her research interests include high-efficiency power amplifiers and transmitters, microwave and millimeter-wave high-performance circuits for communications and radar, medical applications of microwaves, quantum sensing and metrology, and wireless powering. She was the recipient of two IEEE MTT Microwave Prizes for Best Journal Papers, the White House NSF Presidential Faculty Fellow award, the URSI Issac Koga Gold Medal, the ASEE/HP Terman Medal and the German Alexander von Humboldt Research Award. She was elected as foreign member of the Serbian Academy of Sciences and Arts in 2006. She was named IEEE MTT Distinguished Educator in 2013 and the University of Colorado Distinguished Research Lecturer in 2015.